Modeling the Osteogenic Potential of Decellularized Human Bone Particles by Tuning their Size Distribution Through a Sonic Microfragmentation Approach

Alessio Bucciarelli,* Alessandro Pedranz, Laura Gambari, Mauro Petretta, Leonardo Vivarelli, Dante Dallari, Brunella Grigolo, Devid Maniglio,* and Francesco Grassi*

Human decellularized bone fragments are commonly used in clinics to perform allograft surgeries. To reduce the immunological response in the recipient and ensure their safety, these fragments underwent decellularization, a procedure that greatly reduces their osteogenicity (the ability to induce differentiation into osteoblast). In this work, by the introduction of an ultrasonication step to fragment the human bone, the size distribution of the resulting demineralize bone particles can be controlled, tuning their osteogenic potential. The sonication protocol is optimized by a response surface method, using 12 different sonication protocols, allowing to model the relationship between the sonication parameters and the outcoming particles properties in terms of dimensions, physical/chemical properties, and biological activity. The size distribution is extrapolated by a deep learning image segmentation while the structure is characterized by infrared and thermal analysis. The particles are combined with methacrylated silk gel to test in vitro their biological response on adipose-derived stromal cells. The ultrasonication fragmented the bone particles, revealing their internal organic matrix as proved by secondary electron microscopy and confocal microscopy. An inverse linear correlation is found between the particles' sizes and their osteogenic activity, thus proving the efficacy of the proposed ultrasonication treatment in tuning the biological response.

1. Introduction

Bone is a hierarchical complex tissue composed of mineral and organic elements. Structurally, it can be roughly divided into two distinct architectures: cancellous and cortical bone. Cancellous bone is the internal part and is formed by interconnected trabeculae and rods forming a porous material. The direction of the trabeculae maximizes strength specifically for the load that the bone supports. Cortical bone is the outer dense part, composed of osteons, a concentric lamellar structure with a central canal (Haversian canal) that allows the passage of blood vessels. Osteon lamellae comprise aligned collagen fibers arranged in geometric patterns. The fibers are formed by mineralized collagen fibrils in which the organic phase (mostly Type I collagen) and the inorganic phase (nanocrystals of hydroxyapatite, HA) are connected.[1–3]

Bone is continuously remodeled by the combined action of osteoclast and osteoblast. Resorption is performed

A. Bucciarelli, L. Gambari, B. Grigolo, F. Grassi
Laboratorio RAMSES
IRCCS Istituto Ortopedico Rizzoli
Via di Barbiano 1/10, Bologna 40136, Italy
E-mail: Alessio.Bucciarelli@IOR.it; Francesco.Grassi@IOR.it

A. Pedranz, D. Maniglio
Industrial Engineering Department and Biotech Research Center
Italian and European Institute of Excellence on Tissue Engineering and Regenerative Medicine
Via Delle Regole 101, Trento 38123, Italy
E-mail: Devid.Maniglio@unitn.it

M. Petretta
RegenHU SA
Z.I. du Vivier 22, Villaz-St-Pierre 1690, Switzerland

L. Vivarelli, D. Dallari
Reconstructive Orthopaedic Surgery and Innovative Techniques—Musculoskeletal Tissue Bank
IRCCS Istituto Ortopedico Rizzoli
Via Giulio Cesare Pupilli, 1, Bologna 40136, Italy

**ADVANCED
SCIENCE NEWS**

www.advancedsciencenews.com

**ADVANCED
MATERIALS
TECHNOLOGIES**

www.advmattechnol.de

by osteoclasts, multinucleated cells of hematopoietic origin. Bone formation is carried out by osteoblast, cells derived from bone-resident cells of the mesenchymal lineage. The balance between bone resorption and bone production defines healthy tissue; however, when bone resorption is no longer compensated by bone formation, a progressive decline in bone mass arises, which ultimately leads to osteoporosis, a major risk factor for fragility fractures.[4–6]

Bone tissue has a high regenerative ability. Still, injuries or degenerative diseases may cause critical defects that compromise the capacity of self-healing, and the replacement of bone tissue is needed to achieve a full recovery. In considering trauma-induced fractures, it is estimated that up to 10% of all fractures fail to heal within 6 months, a condition known as non-union, causing severe secondary functional deficits in patients.[7]

To support bone regeneration, a large number of procedures and bone substitutes were investigated over the years.[8] Nevertheless, autograft transplantation remains the golden standard since it supports osteoinduction, osteoconduction, and osteogenesis.[9] The efficacy of these is critically linked to the capacity to restore the chemical composition and the biochemical cues typical of the native extracellular matrix in bone.

Autograft tissue can be harvested as cancellous, cortical, and Bone Marrow Aspirate (BMA). Since the transplanted tissue is harvested directly from the patient, it contains the patient cells and consequently, its integration in the injured site has a higher rate of success. However, this method is more painful and has a certain degree of risk. Donor site morbidity is reported in almost 9% of the patients, including but not limited to major complications such as infection, prolonged wound drainage, large hematomas, and reoperation.[10–12] In addition, in some cases, in which the tissue that can be harvested from the patient cannot cover the bone defects, is not a feasible option.[13]

To overcome the limitations of autograft transplantation, researchers and biomedical manufacturers have made significant efforts to develop biomaterials that mimic the properties of autograft. These efforts have primarily involved the use of natural bone, obtained from either allogeneic (human donors) or xenogeneic (animal) sources.[14–17] Among the natural bone grafts, allografts are the most widely used due to their increasing availability from strictly regulated bone tissue banks, their dimensional and functional compatibility, as well as their closer chemical resemblance to the host bone compared to xenografts.[18] This material is available in different forms from both cortical and cancellous bone, as well as massive and osteochondral grafts, to suit surgical needs.[19,20]

One way by which allograft material is provided is decellularized bone particles (dbPTs), usually used as filler for defects in the powdery form obtained by mechanical fragmentation.[21] dbPTs retain both the mineral and extracellular matrix components. This include growth factors and various non-collagenous proteins such as fibronectin, heparan sulfate, dermatan sulfate, chondroitin sulfate, and hyaluronic acid; dbPTs were shown to promote early osteogenesis by Mesenchymal Stromal Cells

(MSC)[22] and to support the osteogenic differentiation of Adipose Stromal Cells (ADSCs).[23] However, the biological responses to allograft are limited by the procedures required to ensure biological safety and prolonged shelf-life, namely freezing and freeze-drying methods.[14,24] Usually, allograft bone compared with autograft one is reported to be less osteoinductive, being less prone to promote the recruitment of immature cells and their differentiation into osteoblasts, but comparably osteoconductive, providing support for the growing of the new tissue including vessels.[16] To overcome these limitations, procedures aiming at improving the osteogenic ability of allograft materials could provide substantial benefits and increase the effectiveness of these approaches.

Interestingly, early work in periodontics provided qualitative and preliminary evidence that the size of bone substitute chips may critically influence the extent of osteogenic differentiation and bone regeneration.[25–27] In the case of hydroxyapatite (the most common synthetic substitute of bone) a reduction in the particle diameter has been proven to be beneficial from the biological viewpoint.[28] However, previous work was based on a limited range of size and never analyzed diameters below 100 μm. Moreover, a reproducible and scalable procedure for bone chips fragmentation has never been described and no studies have been conducted in the case of allograft human bone, the most relevant material in clinical practice.

In this study, we hypothesize that allograft material can be fragmented through a controlled process to achieve a precise dimensional characterization and an improved biological response by bone cells in order to be useful for clinical applications. We established an accurate and controlled novel process of dbPTs fragmentation based on the sequential use of ball milling and probe ultrasonication on bone chips provided by our bone tissue bank (Musculoskeletal Tissue Bank, IRCCS Istituto Ortopedico Rizzoli). Upon producing multiple batches of dbPTs in the low-micrometer range of dimensions (in the order of tens of micrometers), we first applied the use of deep learning semantic segmentation[29–31] of the particles micrographies combined with a Response Surface Method (RSM)[32–36] to evaluate the dimensional reduction and the shape factors of the particles accurately. The fragmented particles were analyzed in terms of morphology by SEM and confocal microscopy, structure using Fourier Transform Infrared Spectroscopy (FTIR), and thermally by Thermo Gravimetric Analysis (TGA). We evidenced a substantial difference in the morphology of the sonicated dbPTs compared to the sole ball-milling, highlighted by filaments of the exposed organic phase. Subsequently, the correlation between dbPTs particle size and biological response was investigated in vitro by confining the particles in a cross-linked hydrogel of methacrylated silk fibroin (Sil-MA) and testing the ability to support osteogenic differentiation of ADSCs.

We proved that ultrasonic fragmentation was beneficial in terms of increasing the osteogenic differentiation of ADSCs. This improvement was almost linearly correlated to the increase in surface area and the decrease in particle size. In addition, the particle fragmentation protocol here proposed is easily implementable and scalable to produce a large amount of material to be used in clinical practice.

**ADVANCED
SCIENCE NEWS**

www.advancedsciencenews.com

**ADVANCED
MATERIALS
TECHNOLOGIES**

www.advmattechnol.de

2. Experimental Section

2.1. Decellularized Bone Powder Preparation and Ultrasonication Treatment

Cortical bone shafts were produced starting from long bones (femur or tibia-harvested from unique human cadaver donors) by personnel of the accredited public non-profit Musculoskeletal Tissue Bank (hereafter BTM) of IRCCS Istituto Ortopedico Rizzoli (Bologna, Italy; EU TE code: IT000096), and stored at −80 °C until further processing. To limit the potential heterogeneity in composition and mechanical properties of human bone depending on donor characteristics, the dbPTs were obtained by cortical bone, which was less susceptible to physiological and pathological changes than trabecular bone.[38] Moreover, the donors were chosen after a screening to exclude donors with pathologies that may compromise the bone structure and to exclude donors outside a determined age range.[39] After the cutting procedure, the cortical shafts were milled at 14 000 rpm with an ultra-centrifugal mill (ZM200, Retsch, Haan, Germany), equipped with a six teeth root and an external sieve with a 1.5 mm cutting diameter. Bone particles were then collected and processed with successive passages in water (for 12–15 h), chloroform (for 72 h), methanol (for 4 h), and hydrogen peroxide (for 2 h) to remove cells, blood, and adipose tissue. After a final wash with sterile water, the decellularized bone particles (dbPTs) were frozen at −80 °C overnight and then freeze-dried (VirTis Genesis 25, SP Scientific, Warminster, PA, USA). Freeze-dried dbPTs were then manually sieved: dbPTs with an average diameter (d) greater than 500 µm were further processed for transplant purposes, and dbPTs smaller than 500 µm were preserved for validation purposes, such as the aim of this study. dbPTs (d< 500 µm) were then subjected to a mechanical fragmentation step through a ball milling device (Mikro Dismembrator S, Sartorius) for 3 min at 2000 rpm; subsequently, dbPTs were mechanically sieved (AS 200, Retsch, Haan, Germany) to sort the fraction within a specific dimension range 50µm<d< 100 µm). The overall process scheme was reported in **Figure 1**A. Briefly, the dbPTs were fragmented by using an ultrasonicator (Hielscher, UP400S, Germany) 50 mg of dbPTs were placed into 20 mL of water in a beaker, stirred at 1500 rpm and simultaneously sonicated, setting the process factors as described in **Table 1**. To verify the influence of the process in the following fragmentation, three factors were considered: the power of the ultrasonicator, its duty cycle, and the time.

2.2. Statistical Methods

A semantic segmentation by deep learning (DL) was used to obtain a quantitative analysis of the SEM images, thus adding a wider range of information with respect to the qualitative assessment usually performed on SEM images. A schematic representation of the segmentation process is shown in **Figure 2**A Fourteen images, comprising a variety of cases, and chosen randomly among the collected micrographs, were manually segmented, and used as a training dataset to train a DL algorithm on an open-source software (APEER, Carl Zeiss, https://www.apeer.com). Then, five SEM images for each of the twelve trials were analyzed by DL to have a significant number of segmented particles

Table 1. Process trial to test the effect of the considered factors on the dbPTs properties. This allowed us to model response equations to predict and properly tune the dbPTs properties.

Trial	Run	Power [%]	Duty [%]	Time [min]
1	7	60	100	10
2	1	100	100	10
3	3	60	50	10
4	2	100	50	10
5	6	60	100	20
6	5	100	100	20
7	4	60	50	20
8	12	100	50	20
9	9	60	100	30
10	11	100	100	30
11	8	60	50	30
12	10	100	50	30

to perform a statistical test. The area of each particle was then detected and used as yield in the following statistical evaluation. The particle diameter was calculated based on the area using the approximation of circular particles of Equation (1) where A is the area.

$$D = 2\sqrt{\frac{A}{\pi}} \tag{1}$$

The descriptive statistic was calculated on both area and diameter distributions, hypothesizing spherical particles of equal diameter, and using the mean and the median diameter values. The equivalent total superficial area was calculated following Equation (2), where D is the equivalent diameter. In this equation, the first term represents the number of particles with an equivalent diameter that fits in 1 mm^3 of material (N) while the second term represents the surface area of each particle (A).

$$A_S = N * A = \left[\frac{10^9}{4/3\pi(D/2)^3}\right] * \left[\pi\left(\frac{D}{2}\right)^2\right] \tag{2}$$

Also, in this case, the approximation of spherical particles was used. The calculation was performed using the equivalent mean diameter and the equivalent median diameter based on the value of the mean and median area, respectively. Based on the used diameter, the total surface area was nominated as A_{S_dmean} or $A_{S\_dmedian}$. The distributions were plotted and resulted to be skewed to the lower values. For this reason, their medians were compared using a Kruskal–Wallis test.

A Response Surface Method (RMS)[32–36] was used to determine the influence of several parameters of the ultrasonication on the dbPTs dimensions, chemical structure, and biological responses. The methodology is schematized in Figure 2B. Three continuous factors were considered, the power level of the ultrasonicator (Factor A), the duty cycle (Factor B), and processing time (Factor C). Other process factors were maintained constant (20 mL water volume, 1500 rpm of the mixer, 50 mg of bone
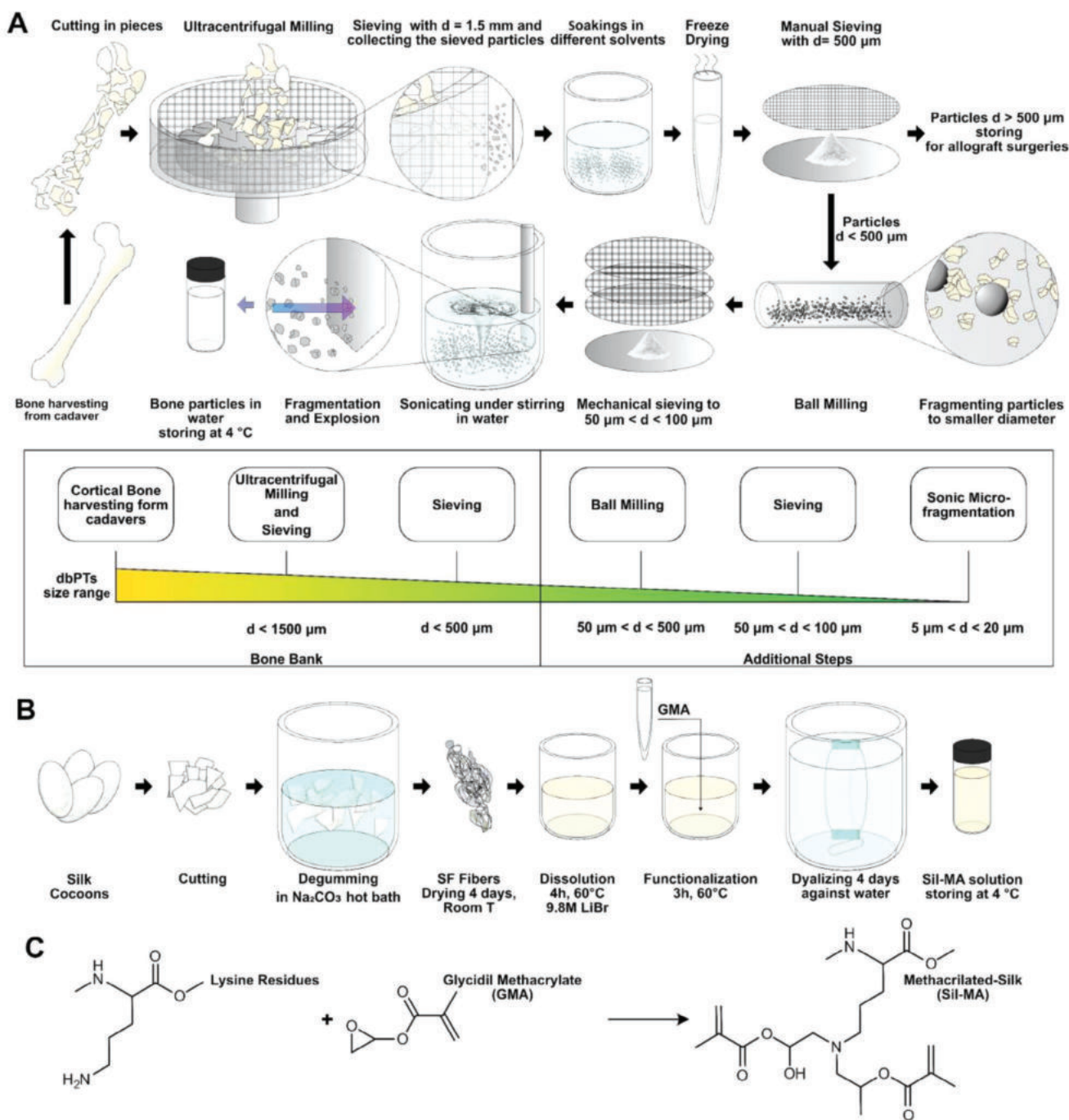
ADVANCED
SCIENCE NEWS

www.advancedsciencenews.com

ADVANCED
MATERIALS
TECHNOLOGIES

www.advmattechnol.de

Figure 1. A) Schematic representation of the decellularized bone particles (dbPTs) production. Bone harvested from cadaver is treated at the bone bank by cutting it into smaller pieces, reduced into particles of 1.5 mm of diameter, and treated with different solvents to remove the donor's cells, blood, and adipose tissue, lyophilized, and manually sieved. The portion of the powder with particles with a diameter below 500 μm was used for the additional steps. Briefly, the powder was ball milled and sieved to obtain a particle's diameter between 50 and 100 μm. This fraction was mixed in water and treated by an ultrasonicator to fragment the particles and expose the organic components. 12 different samples have been produced by performing different protocols of sonication based on different sonication power, duty cycles, and process duration as shown in Table 1. The fragmented bone in water was collected and stored at 4 °C. The additional scheme shows the crucial step in the reduction of the dbPTs dimensions and which fraction was chosen in the different processing phases. dbPTs with dimensions higher than 1500 and 500 μm were not used in the study as currently used as clinical products. The fraction below 500 μm underwent the additional steps. B) Sil-MA preparation scheme. Glycidyl Methacrylate (GMA) was added to silk fibroin (SF) in Lithium Bromide (LiBr) solution under stirring at 60 °C. After 4 h the product was placed in dialysis against water for 4 days. The resultant Sil-MA solution was collected and stored at 4 °C prior to its use. C) Scheme of reaction adapted from Kim et al.,[37] The lysine residues react with the glycidyl groups, allowing the addition of the methacrylic group on the protein chain.
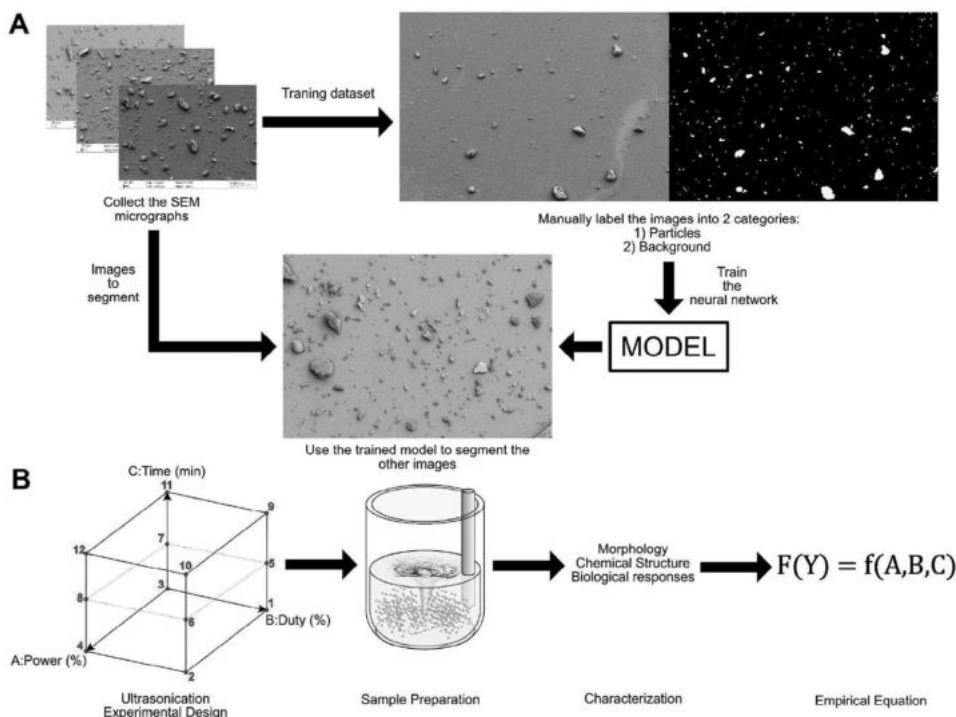
2300635 (4 of 17)

Figure 2. A) Analysis of the SEM images. Five micrographs were collected for all the 12 dbPTs samples obtained with different sonication protocols. A small set of images (14) was used as a training dataset. The images of the training dataset were manually segmented and labeled to distinguish the particles from the background. This data was then used to train the model used to segment the SEM images. B) Experimental design and analysis of the experiment. Three process factors were analyzed (A: sonication power, B: duty cycle, C: Process time), 12 points of the factorial space were chosen, and the respective samples were prepared. The samples were then analyzed in terms of morphology, chemical structure, and biological responses. Empirical model equations of the responses were built by statistical analysis of the collected data.

powder), and uncontrollable factors (i.e., the environmental temperature) were mediated to zero by the randomization of the trials (column 2 of Table 1). From the data collected, empirical equations that relate the dbPTs properties to the process factors were extrapolated. The entire statistical analysis has been done using the programming language R[40] following the statistical strategy described in previous works.[32,35,36,41] An ANOVA test followed by a Tukey multi-comparison was conducted to verify the significance of each term of the reported equation. The levels of significance were assigned as follows: $p \leq 0.1$ (.), $p \leq 0.05$ (*), $p \leq 0.01$ (**), $p \leq 0.001$ (***). The complete model obtainable considering two levels for factor A and B and three levels for factor C is reported in Equation (3). Only the terms with a significant effect ($p \leq 0.1$) were included in the model. The function F has been chosen to both normalize the model residues and to make them patternless. The model was considered significant with a p-value ≤ 0.05. To evaluate the goodness of fit of the model the coefficient of determination (r^2) was calculated. Models with a perfect fitting have an $r^2 = 1$. On the overall dataset, the r^2 index was calculated for each couple of variables and reported as a correlation matrix. The correlation matrix was clustered using as distance of the average.

$$F\ (Y) = c_0\ + c_1 A + c_2 B + c_3 C + c_1 AB + c_1 AC + c_1 BC + c_6 C^2$$
$$+ c_{10} AC^2 + c_{11} BC^2 + c_1 ABC + c_{13} ABC^2 \tag{3}$$

2.3. Morphological Analysis

Field Emission Secondary Electron Microscopy (FE-SEM Supra 40, Carl Zeiss) was used to study the morphology of the processed dbPTs. The solution coming from the ultrasonication was diluted 1:10 in water and resuspended, a 100 µL aliquot was placed in a round lab slide. The water was allowed to evaporate under the hood overnight and then the dbPTs were covered by a 10 nm layer of Platinum/Palladium (Pt/Pd) by sputtering prior to observation. At least five images for each treatment were taken and compared to the unsonicated dbPTs used as reference.

The morphology of the composite made of Sil-MA and sonicated dbPTs was also observed by SEM. The cylinders were placed in liquid nitrogen for a few minutes (to ensure a fragile fracture) and cut with a scalpel to reveal the cross-section. The prepared samples were then covered by sputtering with a 10 nm layer of Pt/Pd prior to their observation.

Confocal Microscopy (Nikon A1, Japan) was used to evaluate the possible exposure of the organic phase by comparing a representative dbPTs sonicated sample with the untreated one to show the particles' morphology and confirm the results obtained by SEM. The samples were prepared by dispersing an equal amount of dbPTs in water solutions and depositing a known volume of each sample in a multiwell. The multiwell was then placed under the hood to evaporate the water and finally observed under the confocal microscope without the addition of dyes or

fluorophores. The particles were excited at 405 and 562 nm collecting two channels: [452–445] nm and [546–593] nm in emission.

2.4. Structural Analysis

Attenuated Total Reflectance Fourier Transform InfraRed spectroscopy (ATR-FTIR, Spectrum one, Perkin Elmer) with an ATR module (ZnSe prism) was used to assert the dbPTs composition. 16 spectra, with a resolution of 1 cm^{-1} for each sample were collected and mediated to obtain an adequate signal-to-noise ratio. The obtained spectra were normalized in the [0,1] range after the baseline correction. To determine the carbonate/phosphorus (C/P) and the amide/phosphorus (Am/P) ratio, Equations (4) and (5), was respectively used, where I indicate the intensity at a specific wavenumber. The IR theoretical penetration in the sample has been roughly estimated by the Equation (6) where ϑ is the incidence angle of the IR beam on the sample, λ_1 is the wavenumber, and n_1 and n_2 are the refractive index of the prism and the sample. The angle of incidence of our instrument was 45 °C, and the refractive index of the ZnSe prism was 2.4 while the generic refractive index for bone was considered, estimated at 1.55.[42]

$$\frac{C}{P} = \frac{I_{1410}}{I_{1010}} \tag{4}$$

$$\frac{Am}{P} = \frac{I_{1648}}{I_{1010}} \tag{5}$$

$$dp = \frac{\lambda_1}{2\pi\sqrt{sin^2\vartheta - \left(n_2/n_1\right)^2}} \tag{6}$$

2.5. Thermal Analysis

TGA (Mettler-Toledo TG50 thermobalance) was conducted in the 25–800 °C range at a 10 °C min^{-1} in the air on a small quantity of particles ≤10 mg inside a hermetically closed pan, to evaluate if there was an influence of the ultrasonication treatment on the thermal response of the dbPTs. The results were reported in Section S4 (Supporting Information).

2.6. Sil-MA Preparation

Sil-MA was prepared following a previously developed protocol[36,37,43,44], which is shown in Figure 1B. *Bombyx mori* silk cocoons were imported from Thailand (Chul Thai Silk Co., Phetchabun, Thailand) and a standard degumming protocol was used to separate SF from silk sericin. Briefly, silk cocoons were cut into pieces of ≈1 cm^2 of area, and placed in a 0.01 м boiling bath of sodium carbonate (Na$_2$CO$_3$, Sigma–Aldrich) for 1 h followed by a second sodium carbonate bath with a lower salt concentration (0.003 м) for another hour. The resultant degummed SF fibers were cleaned from salt residues and progressively taken at room temperature by rinsing them carefully using ultrapure water. Finally, SF was dried for 2 days under

the hood, collected, and stored in a dry environment prior to its use. Then, 4 g of the degummed SF was dissolved into 20 mL of a 9.3 м water solution of LiBr (Sigma–Aldrich) at 60 °C for 4 h in an oven. 1 mL of GMA (Sigma–Aldrich) was added to the SF solution and placed under stirring at 65 °C for 4 h to allow the reaction. To remove the salt and the unreacted GMA, the resulting Sil-MA solution was dialyzed for 4 days against water using a 3.5 kDa dialysis tube. The concentration of the solution (in mg mL^{-1}) was measured using a spectrophotometer (BioSpectrometer basic, Eppendorf), evaluating the intensity of the A280 protein peak (280 nm). The solution was then concentrated (up to 15%), evaporating the water at low temperature using a rotavapor (Eyela N-1110AN) at 70 °C and 300 rpm, checking the concentration from time to time until the desired one was reached. The resultant Sil-MA water solution was then filtered with a 50 µm glass filter and then stored at 4 °C until use. In Figure 1C, the possible reaction pathway is reported showing the results of a previous study which demonstrated that the site for the reaction was the amide side group of lysine amino acid.[37] In the reaction, a primary amide became a di-β-hydroxyamide, through the nucleophilic substitution of nitrogen on one carbon atom of the epoxy ring and the consequent ring opening.

2.7. Sil-MA/dbPTs Composite

Lithium phenyl(2,4,6-trimethylbenzoyl) phosphinate (LAP) was added in the amount of 1% w/v to the Sil-MA water solution. For each of the 12 trials, 300 mg of decellularized bone particles (dbPTs) were added to 600 µL of Sil-MA/LAP solution. 120 µL of suspension were then placed in a 48 multiwell plate and cured with exposure to UV light to form the composite material (360 nm, 1 min). This ensured that the only changing variable was the size of the particles. The volume of Sil-MA solution was the minimum amount to ensure the particle's attachment to the plate, which was a prerequisite to perform the biological trial. The cross-section studied by SEM was 200 µm thick over a surface of 11 000 µm^2 (1.1 cm^2). The particles resulted to be well exposed toward the composite surface (Figure S1, Supporting Information). The multiwell plate with the cured composite material was sterilized prior to performing the cell culture. Sterilization by gamma radiation was performed by Gammatom S.r.l. (Como, Italy), with a dose ranging between 25 and 35 kGy.

2.8. Cell Culture

To investigate the effect of the sonication of the dbPTs on cell proliferation and osteogenic differentiation, commercial ADSCS were employed (Lonza, Switzerland). Upon thawing, cells were expanded in α-MEM 15% FBS at 37 °C, 5% CO$_2$, and 95% O$_2$, and the medium was replaced twice per week. At the start of the experiment, cells were harvested with trypsin/EDTA solution 0,25% (Biochrom, Berlin, Germany) and seeded at a density of 5×10^4 cm^{-2} onto the bone particle composites prior to osteogenic stimulation induction. ADSCs from two different donors were employed in biological tests.

**ADVANCED
SCIENCE NEWS**

www.advancedsciencenews.com

**ADVANCED
MATERIALS**
TECHNOLOGIES

www.advmattechnol.de

2.9. Measurement of Cell Metabolic Activity

To assess the metabolic activity of ADSCs, Alamar Blue assay was employed (Biorad); briefly, the Alamar Blue reagent was prepared according to the manufacturer's instruction (medium depleted of phenol red 10% Alamar Blue) and added to the cells after 48 h and 14 days in culture, by replacing the culture media for 6 h. At the end of the incubation, triplicates of the supernatant were analyzed at the spectrophotometer to measure absorbance at 570 and 600 nm. Cell proteins were quantified by BCA protein assay (Pierce) to normalize the Alamar Blue data. The data were expressed both as total values of cell metabolic activity and values normalized per total cell protein (expressed as Alamar Blue/protein).

2.10. Osteogenic Differentiation and ALP Activity Assay

To induce osteogenic differentiation, ADSCs were cultured for 14 days in an osteogenic medium (α-MEM 20% FBS supplemented with 100 nM dexamethasone, 100 μM ascorbic acid, and 10 mM β-glycerophosphate); which was replaced twice per week. At day 14, the extent of osteogenic differentiation was evaluated by measuring ALP (Alkaline Phosphatase) activity using a commercially available kit (Alkaline Phosphatase Colorimetric Assay Kit, Ab83369, Abcam) following the manufacturer's instructions. Briefly, supernatant was collected, and centrifuged at 200xg, and 100 μL was seeded in triplicates in microplates. p-nitrophenyl phosphate (pNPP) was added to the samples, incubated for 60 min at room temperature (RT), and then the reaction was stopped with a stop solution. Dilutions of pNPP (4-8-12-16-20 nmol) were incubated with ALP enzyme to obtain the standard curve. Absorbance was corrected for the blank of the standard curve. Y nmol of each sample was calculated according to the equation of the standard curve and multiplied for the dilutions' factor. Cell proteins were quantified with BCA protein assay (Pierce). The data were expressed both as total values of ALP and as values normalized per total cell protein (expressed as ALP/protein).

3. Results

3.1. Morphological Analysis of the Powder

The dbPTs' area was evaluated by Image Analysis using a DL approach. **Figure 3**A shows the results of the DL model training and its validation in terms of log(loss), accuracy, and Intersection over Union (IoU). In all cases, the graphs show noisy trends for both the training and the validation, probably due to the small number of images used for the training dataset. However, with the increasing of the training cycles (epoch) we can observe a decrease in the loss and an increase in the accuracy and in the intersection over union (IoU), which, overall, shows a better recognition of the manually segmented features. The DL model was then applied to segment the other images, in Figure 3B,C we report an example of the SEM image and the outcoming segmented image. The DL model worked reasonably well in individuating the dbPTs grains. The model, in most of the cases, was able to exclude

the parts with a morphology that can be attributed to the organic components that were exposed after the dbPTs ruptures obtained by our method. From the analysis of the distributions (Figure 3C as area and Figure 3D as diameter) we could conclude that the ultrasonication protocol was effective in reducing the dimensions of our particles compared to the reference: given that the mean, median, and the higher value of the IQR is higher for the unsonicated dbPTs (Ref) than the 12 dbPTs samples obtained through sonication. The p-values resulting from the statistical comparison were represented as heatmaps. The distributions were almost all statistically different, as highlighted by the heatmaps. This could be expected due to the large number of particles segmented from the SEM images that increase the population number. In terms of mean dimension per particle, the most effective treatment in reducing the dimensions was the 11th. This treatment resulted in a mean diameter per particle of 5.3 μm (area 16.7 μm^2) versus 30 μm (area 94.2 μm) of the unsonicated dbPTs (Ref).

We summarized the descriptive statistics for both area and diameter in Table S9 (Supporting Information). All the distributions (both in case of area and diameter) resulted to be skewed toward the lower values (*skewness>0*) and to be heavily tailed (*kurtosis>3*). The heavy tail is consistent with the fact that 25% of the data point is included in the range between the third interquartile and the maximum and that this range is larger than the interquartile range (IQR, in which 50% of the data points are included).

From the dimensional distributions using the RSM we extrapolated the empirical models of the mean (ANOVA Tables S1, Model Equation S1 and 95% CI coefficients Table S2, Supporting Information) and median (ANOVA Tables S3, Model Equation S2, and 95% CI coefficients Table S4, Supporting Information) diameter and the corresponding standard deviation (ANOVA Tables S5, Model Equation S3, and 95% CI coefficients Table S6, Supporting Information) and interquartile range (ANOVA Tables S7, Model Equation S4, and 95% CI coefficients Table S7, Supporting Information). These models are reported as contour plots in **Figure 4**. As could be expected, both the mean diameter and its standard deviation (StD) decreased by increasing the ultrasonication time and the power range. The same trend can be recognized in the case of median diameter and the associated IQR. Interestingly, the duty cycle resulted to be not significant for all the dimensional responses. The mean diameter resulted to be in the 7.5–30 μm range while StD in the 15–80 μm range. The median diameter was in the 2.5–6.5 μm range and the IQR in the 2.5–22 μm. It should be noted that the StD (and the IQR) should be taken as a measure of the spreading of the diameter distribution. By reducing the StD and the IQR, the ultrasonication process was effectively able to produce smaller particles with more uniform diameters.

A rough calculus of the exposed surface available after each treatment was done by considering a unit of bone volume of 1 μm^3 and dividing it into particles with a volume equal to the mean or the median volume calculated based on the equivalent mean or median diameter of the particles. It should be noticed that this complex treatment of the data allows us to approximately evaluate the free surface area of 3D particles starting from a 2D SEM image. In fact, the area individuated by SEM analysis was only related to the visible part of the particle. By calculating the equivalent volume and then the total superficial area, we were
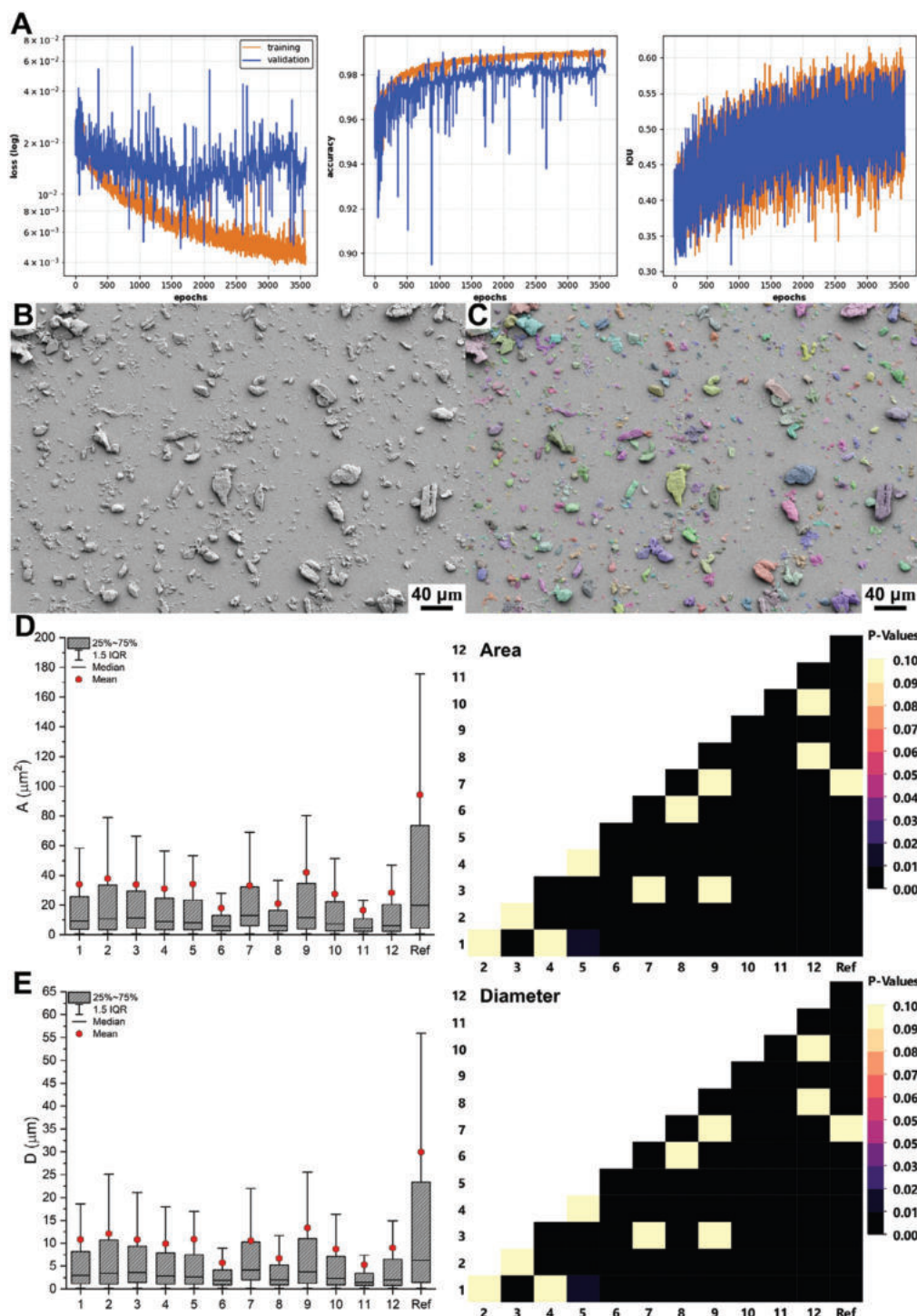
2300635 (7 of 17)

Figure 3. Deep Learning on SEM images and determination of the dbPTs particle dimensions. A) The DL model has been evaluated with different metrics (loss, accuracy, Intersection over Union (IoU)), and both the training and validation have been done on a small image dataset, this is the reason for the noise present in all the metrics. However, a general decrease in loss and a general increase in accuracy and IoU can be observed moving to a higher epoch. This indicates that the model was improving its performance during the training. B) At least five images were collected from each treatment, an example from the first treatment is here reported. C) The DL model applied to the images gave us the segmented image. The area D) and the diameter E) distributions were collected and compared by boxplot. In the boxplots, the distribution histogram (on the right side of the box) was reported. The heatmap on the right side of the boxplot represents the p-value outcome of the Kruskal–Wallis test performed to verify statistically significant differences. Almost all the p-values were below the threshold of $p < 0.05$ implying a statistically significant difference among the groups. Only a few differences resulted in not being statistically significant. As a result, we were able to effectively reduce both the dimension and the dimensional dispersion of the particles compared to the untreated dbPTs (indicated as Ref).
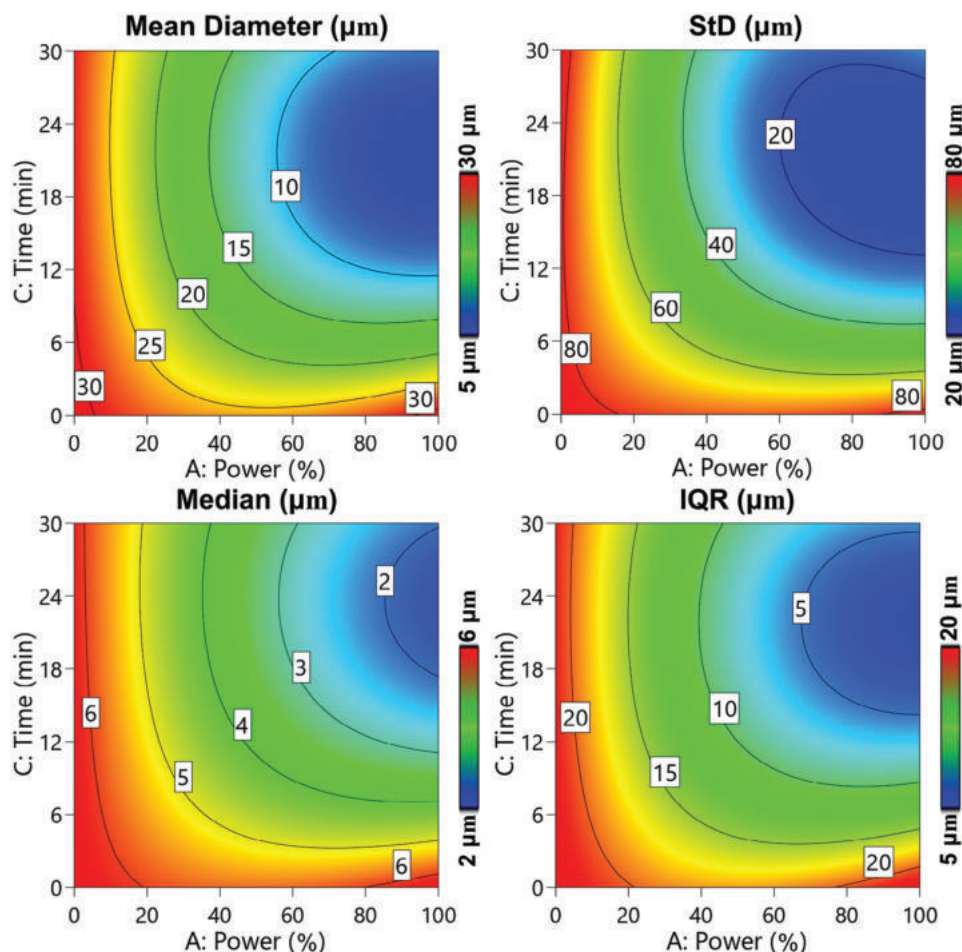
Figure 4. Contour plots of the empirical model of the mean diameter and its standard deviation and the median diameter and the interquartile range (IQR). It should be noted that being the Duty Cycle was not significant it was not reported as a variable, the sizes of the dbPTs were only correlated to the sonication power and time. All the responses decreased with the increase in sonication power and processing time.

able to extract information regarding a 3D spherical object starting from a 2D irregular area. The results are reported in Table S10 (Supporting Information). Compared to the untreated, all the ultrasonication protocols increased the exposed area. In particular, the 11th was the most effective with a surface area almost five times higher than the reference (1132 mm^2 vs 200 mm^2 in case of mean, 4000 mm^2 vs 952 mm^2 in case of median).

From a comparison between the unsonicated and the sonicated dbPTs, we were able to confirm the presence of an organic phase after sonication. As an example, we reported one SEM image of the dbPTs before (**Figure 5**A) and after (Figure 5D) the first sonication procedure (trial 1 in Table 1). In the second figure, the dbPTs appeared to be fragmented and held together by filamentous compounds that we hypothesize to be the remaining organic part of the bone (collagen and morphogenic proteins) after decellularization. This was further confirmed by confocal imaging by comparison of Figure 5B,C,E,F. By comparing the unsonicated sample (Figure 5B) with a sonicated one (Figure 5E, sample 11) the breakage of the particles was clear. At the higher magnification (Figure 5C,F), collagen filaments were visible in the sonicated bone (Figure 5F), highlighted by white arrows, as well as the smaller dbPTs fragment (highlighted by red arrows) while in

the unsonicated dbPTs sample, only dbPTs fragments were visible (Figure 5C, red arrows).

By dispersing these samples in a Sil-MA solution and exposing them to UV radiation, we developed a composite material in which the dbPTs were embedded into a Sil-MA hydrogel matrix. As an example, we report the SEM images of the cross-section of a sample prepared with the powder produced by the first sonication protocol. Figure 5G revealed that the powder was uniformly distributed, as also visible in Figure 5H, while the large cracks indicated a fragile behavior with fractures running toward preferential directions. A higher-magnified image (Figure 5I) confirmed this behavior, highlighting smaller cracks (indicated by green arrows) at the particle-matrix interface.

3.2. Structural Analysis

Structural Analysis was conducted by ATR-FTIR the results are shown in **Figure 6**A. The relative intensity of the peaks has been used to calculate the Carbonate/Phosphorus (C/P, Figure 6B) and the Amine/Phosphorus Ratios (Am/P, Figure 6C). The carbonate, phosphorus, and amine peaks were evaluated at their
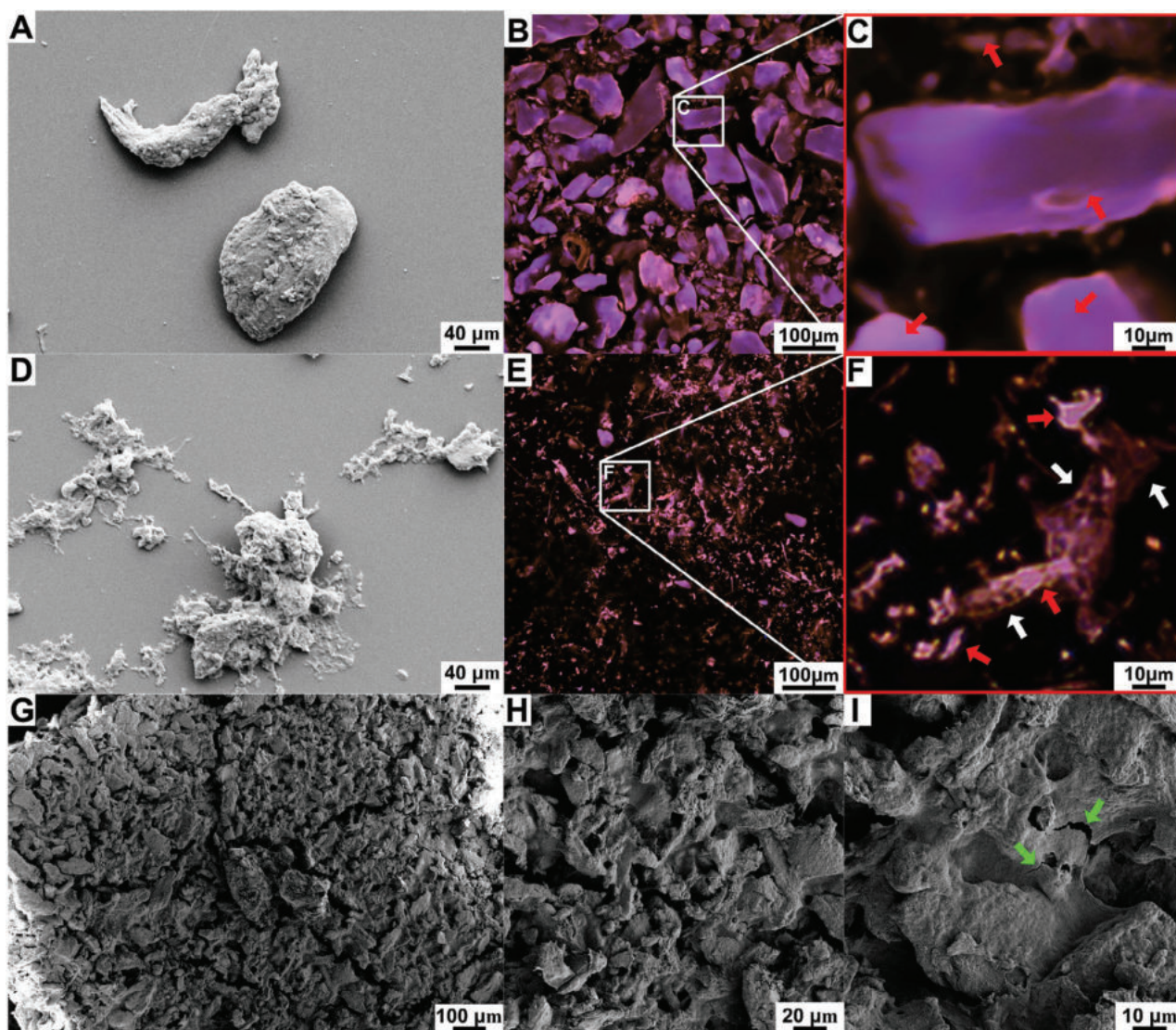
**ADVANCED
SCIENCE NEWS**

www.advancedsciencenews.com

**ADVANCED
MATERIALS
TECHNOLOGIES**

www.advmattechnol.de

Figure 5. SEM and confocal images were taken on A,B,C) the unsonicated powder and D,E,F) the sonicated powder. (C) and (D) Magnified regions of interest in the confocal images. In these images, red arrows show the fragment of bone while white arrows show the exposed organic phase (visible as filaments). The treatment resulted to be effective in revealing the internal organic phase. G,H,I) SEM images at different magnifications of the Sil-MA/fragmented dbPTs composite material. dbPTs resulted in being well dispersed while the fractures present were probably due to interfacial problems between the matrix and the particles. Fractures were highlighted by green arrows.

maximum intensity at 1410, 1010, and 1648 cm^{-1}, respectively. The C/P ratio, as expected, being an index of mineral phases, was not significantly modified by the treatment, as visible from the table reporting the *p*-values of the performed ANOVA test, while statistically significant changes were detected in the case of the Am/P ratio. In fact, in this case, several groups result in a statistically significant difference ($p < 0.05$). In general, the Am/P ratio decreased by the sonication treatments when compared with the unsonicated particles (Figure 6B), this may be due to the degradation of the organic component. Treatments with lower duration (10 min) did not change the Am/P ratio regardless of the setting of the other parameters (treatments 1, 2, 3, and 4). The same effect was obtained by the treatments with longer durations (20 and 30 min) but only when combined with the milder condi-

tions (50% DC, 60% Power, Treatment 7 and 11). The rest of the treatments (5, 6, 8, 9, 10, and 12) had a lower Am/P ratio compared to the reference. Based on this data, we extrapolated a RSM empirical model (Figure 6D; ANOVA Table S11, Supporting Information) based on Equation S5 (Supporting Information) (Coefficient of the equation of the 95% CI in Table S12, Supporting Information). As a general trend, the Am/P ratio decreases with the increase in the processing time and the sonication power.

It should be noted that we were not able to quantify the amount of exposed organic phase but the total amount of collagen, since the IR penetration for our specific crystal (ZnSe) roughly ranges between 0.5 μm (400 cm^{-1}) to 5.03 μm (4000 cm^{-1}) if we consider the refractive index of bone to be 1.55 as previously reported in the literature[42] and using the Equation (4) to evaluate the
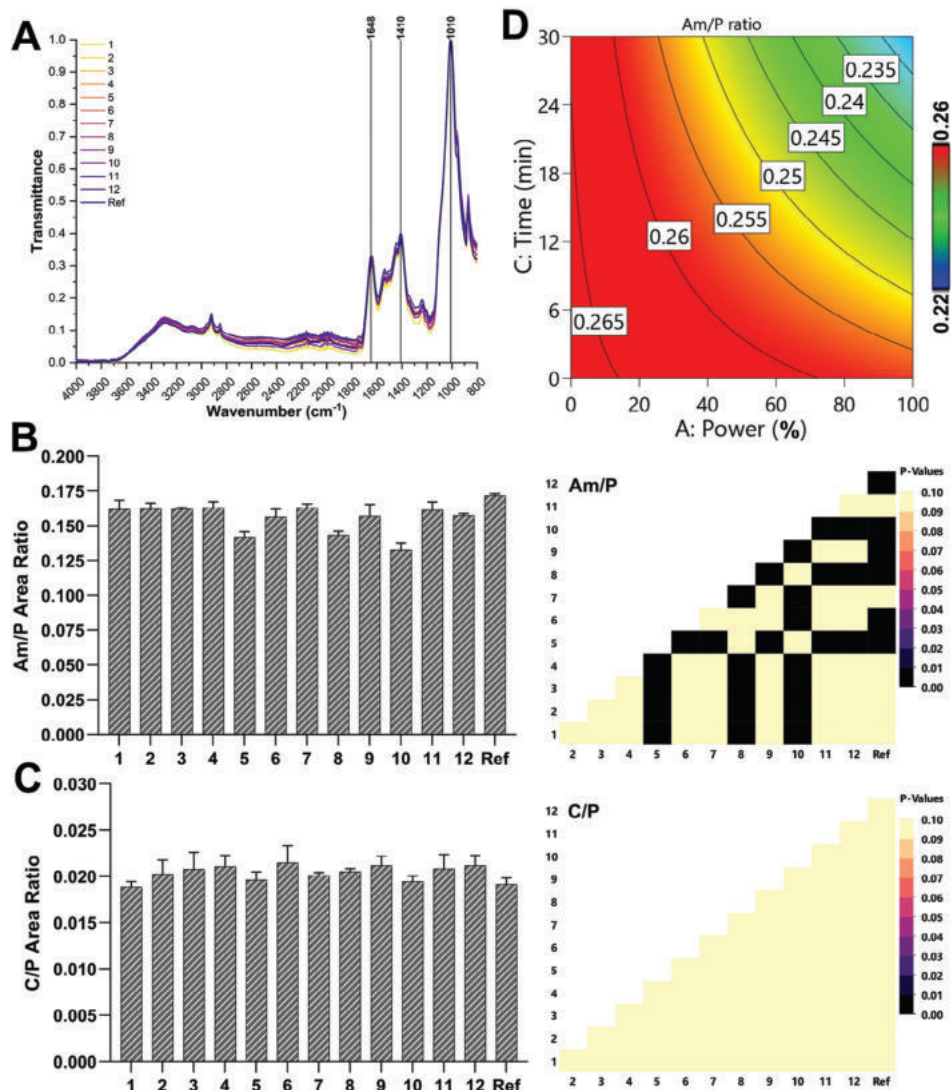
2300635 (10 of 17)

Figure 6. A) ATR-FTIR spectra collected from the resulting dbPTs of the 12 sonication treatments and the reference (Indicated as Ref). The spectra have been base corrected and normalized prior to the successive analysis. B,C)The Am/P and C/P ratios have been calculated from the spectra and reported in panels. For the C/P ratio, no statistical difference was found, while compared to the unsonicated reference, the sonication treatment decreased the Am/P ratio significantly. Other significant differences could be found among the different treatments and shown in the *p*-value heatmap on the right. The Am/P differences allowed us to build an empirical model of its trend and to visualize it as a D) contour plot. The trend was similar to the one observed for the particles' dimensions. As in the previous models in this case the duty cycle resulted to be not significant as reported in the *p*-value heatmap on the right.

penetration depth. We were only able to evaluate the overall effect on the dbPTs structure that resulted in the degradation of the organic phase that occurred during the breaking of the particles and not the amount of exposed organic phase.

3.3. Cell Proliferation and Differentiation

The capacity of dbPTs composites to modulate the behavior of osteoprogenitor cells was first analyzed in a cell proliferation assay. As shown in **Figure 7**, at the early time point of 48 h after seeding, cell proliferation did not significantly change between the different sonication treatments of dbPTs and they do not differ from the unsonicated dbPTs (Ref.) (Figure 7A), suggesting that the procedure of micro fragmentation did not alter the proliferation of cell on the bone dbPTs. However, after 14 days in culture, cell proliferation was significantly different for some of the sonication treatments, as shown in Figure 7B. All the sonicated dbPTs showed higher proliferation rates than the reference (unsonicated sample). However, due to the high variability in the biological responses, the only significantly different response was due to the 11th sonication treatment, which was higher compared to the response of the 1st, 3rd, 4th, 8th, 9th, and 10th treatments and was the only one to be significantly higher than the reference as reported in the *p*-value heatmap.
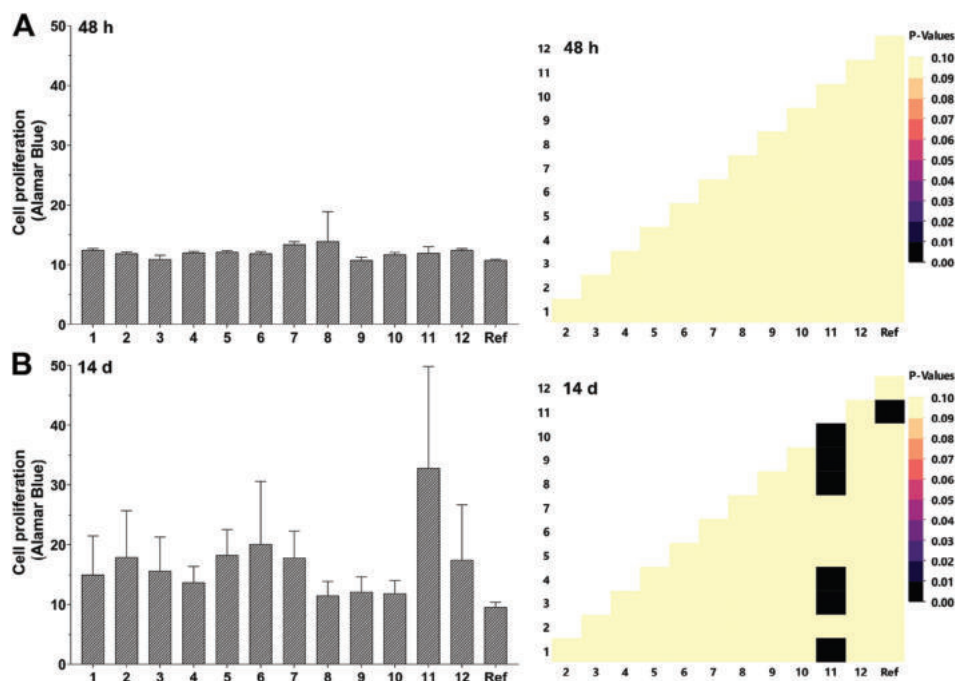
ADVANCED
SCIENCE NEWS
www.advancedsciencenews.com

ADVANCED
MATERIALS
TECHNOLOGIES
www.advmattechnol.de

Figure 7. ADSCs grown under osteogenic conditions were assayed for cellular proliferation after A) 48 h and B) 14 days in culture. The bar graph represents means ± SE of five replicates obtained from two different donors. While after 48 h there was no difference among the different groups (as reported by the p-value heatmap on the right), after 14 days the 11th treatment gave a significantly higher proliferation (as visible in the p-value heatmap on the right). It should be noted that even if in terms of statistical difference, we were not able to reveal significantly different responses (except the one related to group 11), all the treatments resulted in a higher response than the untreated particles (Indicated as Ref).

To get insights into the osteogenic differentiation of ADSCs seeded on bone composites, we measured ALP activity, an assay which is broadly used as a marker for osteogenic differentiation. Notably, ALP plays a crucial role in the first step of mineralization given that it hydrolyzes tissue pyrophosphate and provides inorganic phosphate to promote hydroxyapatite formation and mineralization through hydroxyapatite deposition in ECM. Therefore, ALP production is a good marker of osteogenic differentiation. As shown in **Figure 8**A, ALP activity at the end of the experiment (day 14) was markedly affected by micro fragmentation of dbPTs, as all the values from dbPTs samples were higher than the control, non-sonicated sample (Ref). Moreover, higher values of ALP activity were measured in samples with harsher protocols characterized by smaller size of bone particles (11th and 12th). However, this trend did not achieve statistical significance in the performed ANOVA analyses (as shown by the p-value heatmap). Interestingly, by analyzing the mean values of ALP by RMS we were able to build a significant empirical model (ANOVA Table S13, Supporting Information). The contour plot of the empirical model (Equation S6, Coefficients of the 95% CI in Table S14 (Supporting Information), fitting statistics in Table S15, Supporting Information) is shown in Figure 8C. The trend was similar to the one reported for the dbPTs mean and median dimensions. The ALP increases with the increase of both processing time and sonication power, probably as a consequence of the decrease in the particles' dimensions, as proved by the correlation matrix (**Figure 9**), which reports an almost linear correlation within the decreasing of the dbPTs size. Also, in this case, the change in the duty cycle resulted in no significant effect.

3.4. Correlation Matrix

To verify the hypothesis of higher bioactivity after the sonic micro-fragmentation process, a correlation matrix of the collected dataset was computed as a summary of the overall collected data (Figure 9A). The correlation between couples of variables should be considered significant if r^2 is lower than −0.4 or higher than 0.4. The hierarchical clustering of the matrix by the average method revealed some interesting patterns indicated by black boxes. The biological responses were all to some extent inversely correlated with the mean, and median area of the dbPTs (Mean A and Median A) and directly correlated with the total superficial area (As_dmean and As_dmedian calculated starting from the mean and the median diameter considering 1 mm³ of initial material). Confirming the hypothesis of the increment of the biological activity in correspondence to the decrease of the dbPTs dimensions and the consequent increase of the total superficial area. In some cases, as the Osteogenic differentiation, this correlation was strong, reaching the values of −0.9 (Mean A), and −0.84 (Median A). A slightly lower correlation of these two variables was related to the total superficial area (both As_dmean and As_dmedian), however always higher than 0.6 (moderate). It should be noticed that while the correlation with the dimension is inverse, that with the total superficial area is direct, as could be expected. In the other cases, namely Cell proliferation and Cell proliferation/protein ratio, the correlation was moderate, with values of −0.51 (Mean A), −0.52 (Median A) and −0.47 (Mean A), −0.52 (Median A), respectively. Also in these cases, the reduction in the area was beneficial in terms of biological responses. Other
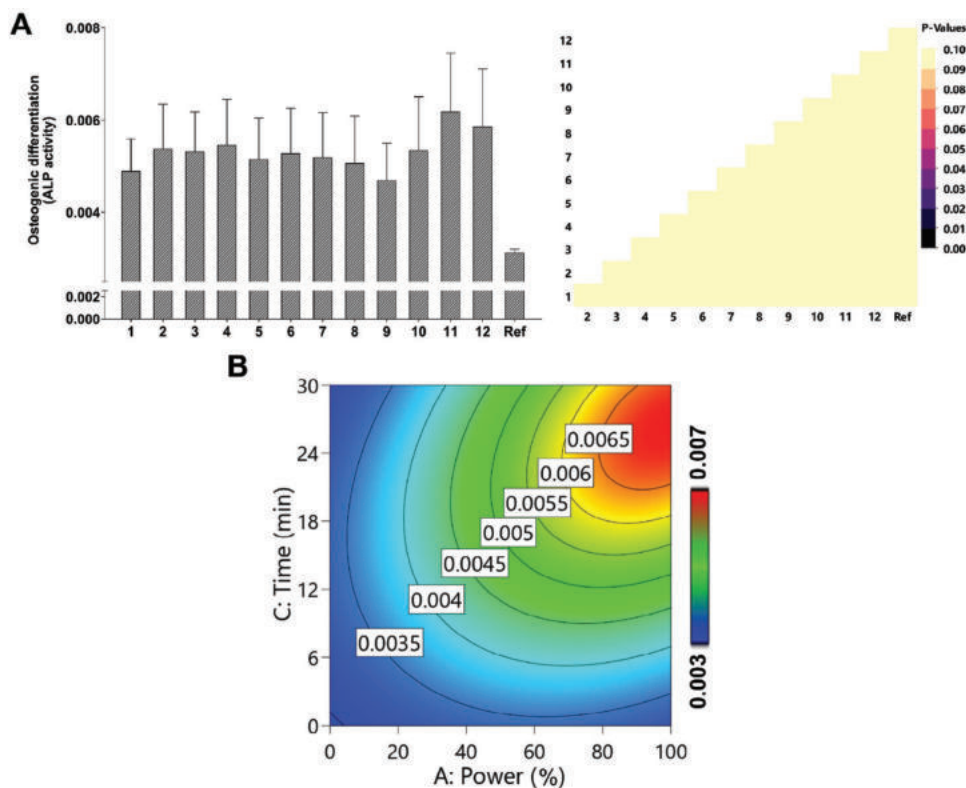
Figure 8. A) ALP activity at the end of the experiment (Day 14) was markedly affected by micro fragmentation of bone particles; Bar graph represents means ± SE of five replicates obtained from two different donors. All the values from BP samples were higher than the reference (unsonicated particles). No significant difference was, however, recorded, as reported by the p-value heatmap on the right B) Contour plot of the empirical model extrapolated by the ALP values. Both the ultrasonication power and time affected the ALP activity as they decreased the dbPTs size and exposed their organic phases.
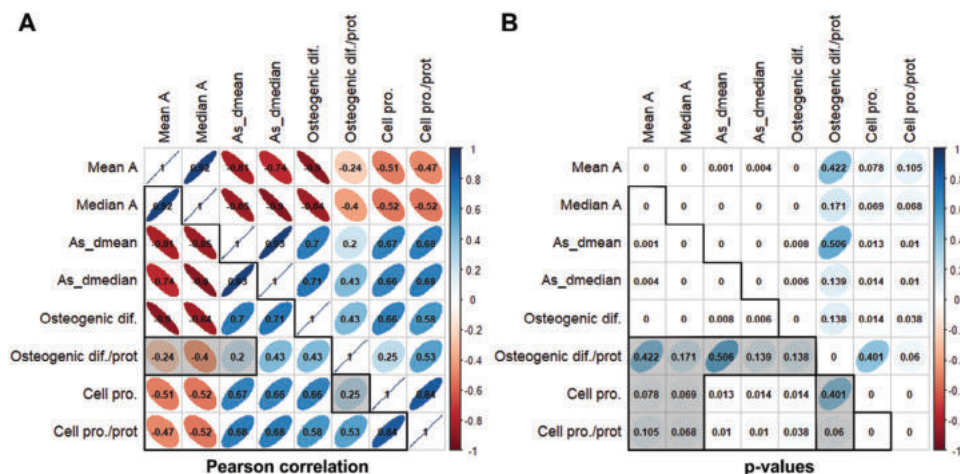
Figure 9. A) Correlation matrix reporting the r^2 index for couples of variables. r^2 defines how strong the linear correlation between the two variables is. −1 represents a perfect inverse linear correlation, and +1 represents a perfect direct linear correlation. Both color and eccentricity variation indicate the value of r^2. Closer the ellipse to a line closer r^2 to the extreme's values. Values below −0.4 and above 0.4 should be considered significant. Insignificant correlations were covered by stripes. Being symmetric, we took into consideration only the lower part of the matrix. Mean A and Median Area represent the mean and the median area of the dbPTs while the As_dmean and As_dmedian are the total superficial area calculated based on the equivalent mean and median diameter respectively as reported in Section 2.2. The Alamar Blue expressed the cell proliferation while the ALP activity the osteogenic differentiation, both considered at day 14 and reported in Section 3.3. The cell proliferation/protein and the Osteogenic differentiation/protein indicate the Alamar Blue and the ALP activity normalized over the cell proteins (which can be interpreted as a normalized value over the number of cells). B) p-values associated with the correlation coefficients, values below 0.05 were considered statistically significant. For the sake of clarity, p-values lower than 0.001 were reported as 0. Not all the significant correlations resulted to be statistically significant.

**ADVANCED
SCIENCE NEWS**

www.advancedsciencenews.com

**ADVANCED
MATERIALS
TECHNOLOGIES**

www.advmattechnol.de

interesting moderate direct correlations are between the Osteogenic differentiation with Cell proliferation (0.66) and the Cell differentiation/protein ratio with Osteogenic differentiation/protein ratio (0.53), which overall indicates that the cells differentiate through the osteogenic pathway.

The p-values of the correlation matrix were computed and reported in Figure 9B, in this case, correlations with a p-value below 0.05 should be considered as statistically significant. Interestingly not all correlations spotted in Figure 9A were statistically significant. In particular, the cell proliferation and the cell proliferation/protein ratio were significantly correlated only with the increase in the surface area, which is an indirect effect of the particle size reduction. The Osteogenic differentiation was instead strongly correlated with the decrease in the particle size and the increase in the total area.

4. Discussion

The size of dbPTs used in allograft procedures may critically influence the extent of osteogenic differentiation and thus bone regeneration. In this work, we developed a method to reduce the dimension of human bone particles through a controlled and scalable process, which allowed us to model the relationship between size and the resulting osteogenic differentiation.

The work is based on human cortical bone tissue provided by the Musculoskeletal Tissue Bank of the Rizzoli Orthopaedic Institute. Usually, the materials with a size larger than 500 μm are assigned to clinical purposes while the smaller fraction (size in the 50–500 μm range) is discarded. Here, we exploited the use of this smaller fraction by performing a ball milling, sieving, and a sonication process to further reduce its mean size to a range between 5 and 20 μm.

It should be noticed that while the smaller sieve had a cutting edge of 50 μm a portion of the equivalent diameter distribution was above this value (as noticed by the maximum equivalent diameter recorded of the unsonicated sample, Table S9, Supporting Information). This can be explained by considering the fact that dbPTs were fragmented in irregular shapes. So, particles with some of their dimensions lower than the cutting diameter could pass throughout the sieve, and being the equivalent diameter based on the assumption of a circular particle, the resulting value was higher than 100 μm.

To systematically analyze the importance of particle size, we employed an ultrasonication-based approach. This was performed using an RSM method,[44–47] strategically producing 12 different batches of dbPTs varying the three main process factors (the sonication power, the process time, and the duty cycle). RMS does not require the knowledge of the physics regulating the process. The process is treated as a black box in which the process factors are changed strategically to guarantee the possibility of statistically analyze the outcoming data from the selected yields.[46,47] In our specific case, we must consider that the distance of each particle from the sonotrode is variable, due to the rotation at a constant RPM of the water containing the particles. Besides this, dbPTs contain entrapped air that may interact with the sonic wave as well. Consequently, the physics of the system is not easily describable.

In terms of particle size, we were able to determine the dbPTs size distributions by semantic segmentation of the collected SEM micrographs.[30,31,48] Interestingly, the decrease in the dimension of the particles is not straightforward to understand. In fact, the 11th treatment (60% of power, 50% duty, and 30 min) gave the smaller particles and the best results in terms of biological responses while the harshest treatment was the 10th (100% of power, 100% duty, and 30 min). This demonstrates that even a relatively simple process as the sonication step here discussed is indeed quite complex to describe, with several factors interacting. In general, we observed a decrease in the diameter due to the ultrasonication process. In fact, all 12 treatments resulted in distributions with smaller sizes than the unsonicated sample. The RSM analysis revealed that during the sonication, both time and power were important in decreasing the dbPTs dimensions (mean and median) and improving their homogeneity (reducing their StD and IQR). On the contrary, the duty cycle (in the considered range) was not a significant parameter. To our knowledge, only a few studies report the use of ultrasonication applied to mineral fragmentation[49–52] and no one is applied to materials that contain both minerals and organic components. However, all of them clearly report an almost linear decrease in the particles' dimensions with process time,[49–52] which was also found in our study.

Interestingly, the particles' morphology observed by SEM and the confocal imaging seems to be different in the case of ball milling fragmentation (shown in Figure 5A–C) and sonication (in Figure 5D,C,E). In addition, the particles' morphology was different from what is reported in the literature in the case of ultrasonication of synthetic hydroxyapatite[53] and other minerals.[49–52] The minerals particle breakage, induced by sonication, was previously explained by the effect of the stable cavitation bubbles formed in the low range frequency (20–50 kHz, our instrument works at 24 kHz).[49,54] These bubbles, generated by pressure differences in the system and containing vapor and dissolved gasses, when collapsing generate extreme conditions (pressure above 500 bar) that lead to shear forces able to break even hard materials.[55,56] In addition to this phenomenon, we can hypothesize that the sonication also affected the air bubbles entrapped inside the bone[57] starting the fracture from dbPTs core, generating the morphology that we observed. In addition, we could observe the presence of organic structures, which were not visible prior to sonication.

The FTIR was used to understand how the sonication treatment affected the bone chemical structure. As expected, the phosphate-calcium ratio was unaffected by the process, while the amine-phosphate ratio decreased with the increase in sonication power and time. The trend studied by RMS (Figure 6D) was almost the same as the one recorded in the case of the particles' dimensions (Figure 4). This may indicate a partial degradation of the organic matrix that occurred during the fragmentation as previously reported in the case of bone treatment with chemicals.[58] However, in our case, the organic matrix degradation is compensated by its improved accessibility.

In the Differential TGA (DTGA, reported in the Supporting Information) the same peaks were found before and after sonication but with a lower intensity that may confirm the result obtained by FTIR (Section S4, Supporting Information). Not all the components were recognizable due to the complexity of the natural tissue and, even if they were detected in previous studies, they remain not assigned.[59,60] Quantitatively, the final residue in

the range of 36%–39% was in accordance with a previous study (35.6% and 36.4%).[61]

A preliminary in vitro evaluation was performed by combining dbPTs in a cross-linked hydrogel of Sil-MA, which was also proved to support osteogenesis.[62] The use of silk has been chosen specifically for its biocompatibility, tunable biodegradability, and the presence of sites for cell adhesion,[1,63,64] and may be regarded as a good alternative to the clinically used poloxamer.[48,65] The in vitro evaluation revealed an enhanced proliferation (evaluated by Alamar Blue assay) for the sample with the smaller diameter only at day 14, while after 48 h no difference among the samples was recorded (Figure 7). A similar effect was previously reported for synthetic nanohydroxyapatite, where a lower particle dimension enhanced osteoblast proliferation.[66,67] In terms of differentiation, the samples with smaller diameters ensured a higher biological response, as determined by the ALP assay (Figure 8). In this case, we were also able to model the ALP response based on the process parameters (Figure 8B). The trend of the increase of the ALP response was similar to the decreasing trend of the particle size (Figure 4). This is also the underlying reason for their proved almost inverse linear correlation, and the linear correlation with the total exposed surface. In literature, an effect related to the particles' size was detected also for synthetic nano-hydroxyapatite on human osteoblast. In this case, a reduction in the size inhibited the cell apoptosis and promoted the cells' growth[66,67] and differentiation.[68] The same effect was reported in early qualitative studies conducted on humans[25–27] in which it was hypothesized that a reduction in the dbPTs dimensions may be beneficial in terms of tissue regeneration, without proving this point.

Our findings substantiate those early observations: improved osteogenic response, as measured by ALP activity, is likely caused by an increased exposure of surface-bearing collagenous and non-collagenous proteins, a key component of the native bone extracellular matrix. Indeed, we show that a finely tuned protocol of ultrasonication can increase the exposed surface of the bone particles by as much as five times. To our knowledge, this is the first proof-of-concept proposing a workflow for processing allograft tissue, the size of bone particles, and the resulting osteogenic response by osteoprogenitor cells. We expect that this protocol may be used by bone tissue banks and manufacturers to produce bone-derived products with improved biological performances; or applications in preclinical studies involving the use of dbPTs in bone tissue engineering applications.

However, this work has several limitations. It is based on dbPTs derived from the cortical bone of a single donor. Further studies based on several donors and different harvesting sites of bone should be performed to ensure the protocol robustness against the natural variability of the material. This will ensure obtaining comparable properties for different sonicated dbPTs batches and thus reliable translation toward the application on patients. Further, preclinical in-vitro and in-vivo studies will be required to better understand the advantages and disadvantages of micrometric bone particles compared to the clinically used bone particles (d > 500 μm). In addition, only a small amount of bone has been treated in each sonication procedure, and hence a scale-up to a greater quantity would be required to effectively apply this protocol to a production site as bone tissue banks. This would re-quire an optimization of the process geometry and probably the development of a sonication reactor.

5. Conclusion

In this work, we produced dbPTs from allograft bone harvested from a human donor, with improved biological activity by adding an ultrasonication step to the workflow of production. Notably, we used dbPTs discarded from the classical protocol of production of bone for transplantation, thus providing a proof-of-principle of their potential use. The morphological and dimensional analysis demonstrated that the sonication was effective in reducing the particles' dimensions and exposing the organic components, differently to other techniques such as ball milling. We hypothesize that being the morphology of the dbPTs different from what observed for other techniques applied to the same material (ball milling, centrifugal milling), and from the sonication of other minerals, the bone may be fragmented from the core, as well as from the surface. The process was completely characterized by a response surface method that allowed us to determine which sonication parameters most efficiently influenced the biological response. A clear correlation, not proven before, was identified between the particle size and the biological response. Even if we were not able to quantify the exposed organic matrix, we hypothesize that higher fragmentation led to higher exposure and thus a better biological response. An evaluation of the donor-to-donor variability should be performed to better understand its impact on the final material, and further in vivo experiments will be necessary to evaluate the effectiveness of the optimized fragmentation protocol in promoting tissue regeneration. In conclusion, being a simple and known technological platform, sonication may be adopted by bone banks and manufacturers to produce bone-derived products with improved biological performances. In addition, this process may be suitable also for large material production using commercially available ultrasonicator reactors.

Supporting Information

Supporting Information is available from the Wiley Online Library or from the author.

Conflict of Interest

The authors declare no conflict of interest.

Author Contributions

A.B. performed conceptualization; designed methodology; performed validation and formal analysis; visualized the idea for the study; wrote the

ADVANCED
SCIENCE NEWS

www.advancedsciencenews.com

ADVANCED
MATERIALS
TECHNOLOGIES

www.advmattechnol.de

[1] A. Bucciarelli, A. Motta, *Biomaterials Advances* **2022**, *139*, 212982.
[2] M. J. Olszta, X. Cheng, S. S. Jee, R. Kumar, Y.-Y. Kim, M. J. Kaufman, E. P. Douglas, L. B. Gower, *Mater. Sci. Eng.: R: Rep.* **2007**, *58*, 77.
[3] H. P. Schwarcz, D. Abueidda, I. Jasiuk, *Front. Phys.* **2017**, *5*.
[4] G. A. Rodan, *Bone* **1992**, *13*, S3.
[5] R. Florencio-Silva, G. R. D. S. Sasso, E. Sasso-Cerri, M. J. Simões, P. S. Cerri, *Biomed. Res. Int.* **2015**, *2015*, 421746.
[6] Y. Han, X. You, W. Xing, Z. Zhang, W. Zou, *Bone Res.* **2018**, *6*, 16.
[7] D. Saul, M. M. Menger, S. Ehnert, A. K. Nüssler, T. Histing, M. W. Laschke, *Bioengineering* **2023**, *10*, 85.
[8] A. Wubneh, E. K. Tsekoura, C. Ayranci, H. Uludag, *Acta Biomater.* **2018**, *80*, 1.
[9] W. Wang, K. W. K. Yeung, *Bioact Mater* **2017**, *2*, 224.
[10] H. Schaaf, S. Lendeckel, H.-P. Howaldt, P. Streckbein, *Oral Surg Oral Med Oral Pathol Oral Radiol Endod.* **2010**, *109*, 52.
[11] G. Tonk, P. K. Yadav, S. Agarwal, K. Jamoh, *JOTR* **2022**, *29*, 221049172210921.
[12] R. Pollock, I. Alcelik, C. Bhatia, G. Chuter, K. Lingutla, C. Budithi, M. Krishna, *Eur Spine J.* **2008**, *17*, 845.
[13] T. Boyce, J. Edwards, N. Scarborough, *Orthop. Clin. North Am.* **1999**, *30*, 571.
[14] P. Baldwin, D. J. Li, D. A. Auston, H. S. Mir, R. S. Yoon, K. J. Koval, *J. Orthop Trauma* **2019**, *33*, 203.
[15] Z. Amini, R. Lari, *Tissue Cell* **2021**, *69*, 101494.
[16] Y. Fillingham, J. Jacobs, *Bone Joint J.* **2016**, *98-B*, 6.
[17] M. Govoni, L. Vivarelli, A. Mazzotta, C. Stagni, A. Maso, D. Dallari, *Materials* **2021**, *14*, 3290.
[18] G. Graziani, M. Govoni, L. Vivarelli, M. Boi, M. De Carolis, M. Bianchi, E. Sassoni, M. C. Bignozzi, G. Carnevale, F. Marmi, M. C. Maltarello, D. Dallari, *Coatings* **2020**, *10*, 522.
[19] S. N. Khan, F. P. Cammisa, H. S. Sandhu, A. D. Diwan, F. P. Girardi, J. M. Lane, *J. Am. Acad. Orthop. Surg.* **2005**, *13*, 77.
[20] T. Roberti Di Sarsina, M. Fiore, V. Coco, M. Govoni, L. Vivarelli, N. Rani, N. Del Piccolo, D. Dallari, *Life.* **2021**, *11*, 1205.
[21] E. Steijvers, A. Ghei, Z. Xia, *Biomater. Transl.* **2022**, *3*, 65.
[22] Y. Hashimoto, S. Funamoto, T. Kimura, K. Nam, T. Fujisato, A. Kishida, *Biomaterials* **2011**, *32*, 7060.
[23] M. Fröhlich, W. L. Grayson, D. Marolt, J. M. Gimble, N. Kregar-Velikonja, G. Vunjak-Novakovic, *Tissue Eng Part A* **2010**, *16*, 179.
[24] F. R. Grassi, R. Grassi, L. Vivarelli, M. Dallari, M. Govoni, G. M. Nardi, Z. Kalemaj, A. Ballini, *Materials* **2020**, *13*, 1393.
[25] A. F. Rivault, P. D. Toto, S. Levy, A. W. Gargiulo, *J. Periodontol.* **1971**, *42*, 787.
[26] R. E. Robinson, *J. Periodontol* **1969**, *40*, 503.
[27] C. A. Shapoff, G. M. Bowers, B. Levy, J. T. Mellonig, R. A. Yukna, *J. Periodontol* **1980**, *51*, 625.
[28] J.-S. Sun, H.-C. Liu, W. Hong-Shong Chang, J. Li, F.-H. Lin, H.-C. Tai, *J. Biomed. Mater Res.* **1998**, *39*, 390.
[29] F. Lateef, Y. Ruichek, *Neurocomputing* **2019**, *338*, 321.
[30] P. Monchot, L. Coquelin, K. Guerroudj, N. Feltin, A. Delvallée, L. Crouzier, N. Fischer, *Nanomaterials* **2021**, *11*, 968.
[31] A. B. Oktay, A. Gurses, *Micron* **2019**, *120*, 113.
[32] A. Bucciarelli, S. Chiera, A. Quaranta, V. K. Yadavalli, A. Motta, D. Maniglio, *Adv. Funct. Mater.* **2019**, *29*, 1901134.
[33] A. Gaiardo, D. Novel, E. Scattolo, M. Crivellari, A. Picciotto, F. Ficorella, E. Iacob, A. Bucciarelli, L. Petti, P. Lugli, A. Bagolini, *Sensors* **2021**, *21*, 783.
[34] J. K. W. Lam, Y. Xu, A. Worsley, I. C. K. Wong, *Adv. Drug Deliv. Rev.* **2014**, *73*, 50.
[35] A. Bucciarelli, A. Adami, C. R. Chandaiahgari, L. Lorenzelli, presented at 2020 IEEE Int. Conf. on Flexible and Printable Sensors and Systems (FLEPS), IEEE, Piscataway, NJ **2020**.
[36] A. Bucciarelli, T. Muthukumar, J. S. Kim, W. K. Kim, A. Quaranta, D. Maniglio, G. Khang, A. Motta, *ACS Biomater. Sci. Eng.* **2019**, *5*, 6374.
[37] S. H. Kim, Y. K. Yeon, J. M. Lee, J. R. Chao, Y. J. Lee, Y. B. Seo, M. T. Sultan, O. J. Lee, J. S. Lee, S.-I. Yoon, I.-S. Hong, G. Khang, S. J. Lee, J. J. Yoo, C. H. Park, *Nat Commun.* **2018**, *9*, 1.
[38] S. M. Ott, *Am J. Nephrol* **2018**, *47*, 373.
[39] H. H. Bayraktar, E. F. Morgan, G. L. Niebur, G. E. Morris, E. K. Wong, T. M. Keaveny, *J. Biomech.* **2004**, *37*, 27.
[40] R. C. Team, *R: A Language and Environment for Statistical Computing*, Scientific Research, Vienna, Austria. **2019**.
[41] A. Bucciarelli, C. Reddy Chandraiahgari, A. Adami, V. Mulloni, L. Lorenzelli, *Flex. Print. Electron.* **2020**, *5*, 045002.
[42] E. A. Genina, A. N. Bashkatov, V. V. Tuchin, *Adv. Opt. Technol.* **2008**, 267867.
[43] D. N. Rockwood, R. C. Preda, T. Yücel, X. Wang, M. L. Lovett, D. L. Kaplan, *Nat. Protoc.* **2011**, *6*, 1612.
[44] A. Bucciarelli, G. Greco, I. Corridori, N. M. Pugno, A. Motta, *ACS Biomater. Sci. Eng.* **2021**, *7*, 1374.
[45] A. M. Bossi, A. Bucciarelli, D. Maniglio, *ACS Appl. Mater. Interfaces* **2021**, *13*, 31431.
[46] J. Antony, *Design of Experiments for Engineers and Scientists*, Elsevier, Amsterdam, Netherland **2003**.
[47] D. C. Montgomery, *Design and Analysis of Experiments*, 8th Ed., Technometrics, United Kingdom **2012**.
[48] P. Zarrintaj, J. D. Ramsey, A. Samadi, Z. Atoufi, M. K. Yazdi, M. R. Ganjali, L. M. Amirabad, E. Zangene, M. Farokhi, K. Formela, M. R. Saeb, M. Mozafari, S. Thomas, *Acta Biomater.* **2020**, *110*, 37.
[49] J. Jordens, T. Appermont, B. Gielen, T. Van Gerven, L. Braeken, *Cryst Growth Des.* **2016**, *16*, 6167.
[50] V. Raman, A. Abbas, *Ultrason. Sonochem.* **2008**, *15*, 55.
[51] O. Y. Toraman, H. Inal, *Part. Sci. Technol.* **2017**, *35*, 627.
[52] S. S. Arvapalli, M. Miryala, M. Jirsa, M. Murakami, *Supercond. Sci. Technol.* **2020**, *33*, 115009.
[53] L. A. Párez-Maqueda, F. Franco, M. A. Avilés, J. Poyato, J. L. Pérez-Rodríguez, *Clays Clay Miner.* **2003**, *51*, 701.
[54] Y. Chen, V. N. T. Truong, X. Bu, G. Xie, *Ultrason. Sonochem.* **2020**, *60*, 104739.

[55] C. N. Cheaburu-Yilmaz, H. Y. Karasulu, O. Yilmaz, *Polymeric Nanomaterials in Nanotherapeutics*, Elsevier, Netherland **2019**, 437.

[56] X. Wang, X. Wang, J. Wang, Z. Tian, *Appl. Sci.* **2020**, *10*, 5868.

[57] E. Soldati, M. Pithioux, D. Guenoun, D. Bendahan, J. Vicente, *Diagnostics* **2022**, *12*, 439.

[58] A. P. Mamede, A. R. Vassalo, E. Cunha, D. Gonçalves, S. F. Parker, L. A. E. Batista De Carvalho, M. P. M. Marques, *RSC Adv.* **2018**, *8*, 27260.

[59] F. Miculescu, G. E. Stan, L. T. Ciocan, M. Miculescu, A. Berbecaru, I. Antoniac, *Dig. J. Nanomater. Biostructures* **2012**, *7*, 1667.

[60] L. F. Lozano, M. A. Peña-Rico, A. Heredia, J. Ocotlán-Flores, A. Gómez-Cortés, R. Velázquez, I. A. Belío, L. Bucio, *J. Mater. Sci.* **2003**, *38*, 4777.

[61] J. J. Lim, *J Biol Phys* **1975**, *3*, 111.

[62] A. Bucciarelli, M. Petretta, B. Grigolo, L. Gambari, A. M. Bossi, F. Grassi, D. Maniglio, *Gels* **2022**, *8*, 833.

[63] B. Kundu, R. Rajkhowa, S. C. Kundu, X. Wang, *Adv. Drug Deliv. Rev.* **2013**, *65*, 457.

[64] L.-P. Yan, J. M. Oliveira, A. L. Oliveira, S. G. Caridade, J. F. Mano, R. L. Reis, *Acta. Biomater.* **2012**, *8*, 289.

[65] H. Zhang, L. Yang, X.-G. Yang, F. Wang, J.-T. Feng, K.-C. Hua, Q. Li, Y.-C. Hu, *Orthop. Surg.* **2019**, *11*, 725.

[66] Y. Cai, Y. Liu, W. Yan, Q. Hu, J. Tao, M. Zhang, Z. Shi, R. Tang, *J. Mater. Chem.* **2007**, *17*, 3780.

[67] Z. Shi, X. Huang, Y. Cai, R. Tang, D. Yang, *Acta Biomater.* **2009**, *5*, 338.

[68] S. Dasgupta, S. Tarafder, A. Bandyopadhyay, S. Bose, *Mater. Sci. Eng., C* **2013**, *33*, 2846.